Radiometric Calibration of the VIIRS Reflective Solar Bands with Robust Characterizations and Hybrid Calibration Coefficients

Junqiang Sun[1,2] and Menghua Wang[1]

[1]NOAA National Environmental Satellite, Data, and Information Service,
Center for Satellite Applications and Research, E/RA3,
5830 University Research Ct., College Park, MD 20740, USA
[2]Global Science and Technology, 7855 Walker Drive, Suite 200, Greenbelt, MD 20770, USA

Applied Optics
Resubmitted on 9/20/2015

ABSTRACT

The Visible Infrared Imaging Radiometer Suite (VIIRS) is now entering its fourth year of on-orbit global environmental observation producing a wide range of science output. The ocean color products in particular requires a level of accuracy from the reflective solar bands (RSB) that is a magnitude higher than the specification. In this work we present an updated and completed core calibration pipeline that achieves the best sensor data records (SDR) to date and helps the ocean color products to reach maturity. We review the core calibration methodology of the RSB and describe each essential input, including solar diffuser stability monitor (SDSM), solar diffuser (SD) and lunar calibrations. Their associated issues along with the successful mitigation and improved results are described and presented. In particular, we illuminate the inaccuracy suffered due to the evolving angular dependence in the degradation of the on-board SD that impacts the heart of the RSB calibration, but that lunar-based calibration instead provides the correct long-term baseline for the successful restoration of the core methodology.

The new look-up-tables (LUTs), combining the coefficients from the SD-based and lunar-based calibrations, produces the optimal result with an estimated accuracy of ~0.2%. This hybrid approach highlights significant progress in the VIIRS RSB calibration and marks a completion of the core calibration result upon which other physical impacts or scientific issues can then be more accurately examined. We demonstrate the significant improvement and its impact on the ocean color products by comparing the current official output to the newly generated result. Lastly, we point out that this hybrid calibration coefficients scheme is made possible by a VIIRS design and layout change over its predecessor, the Moderate Resolution Imaging Spectroradiometer (MODIS) allows both the SD and the Moon to be viewed by the RSB at the same angle of incidence (AOI). Thus, this design element warrants serious consideration for other satellite sensors utilizing similar calibration methodology.

Keywords: VIIRS, Reflective Solar Bands, Solar diffuser, Solar diffuser stability monitor, Moon, Ocean color remote sensing

1. Introduction

The Visible Infrared Imaging Radiometer Suite (VIIRS) is one of five instruments housed by the Suomi National Polar-orbiting Partnership (SNPP) satellite launched on October 28, 2011 [1-2], and has expectedly become the primary instrument for observations of global climate phenomena. VIIRS has 22 spectral bands covering a spectral range from 0.410 to 12.013 μm, which include 14 reflective solar bands (RSB), 7 thermal emissive bands (TEB), and a panchromatic day/night band (DNB). The VIIRS RSB are calibrated on-orbit with an on-board solar diffuser (SD) [3-5], whose performance and degradation is itself tracked by a solar diffuser stability monitor (SDSM) [6-9]. The VIIRS RSB on-orbit changes are also monitored with scheduled monthly lunar observations through the instrument's space view (SV) port [9-12], which is also used to provide the instrument's dark scene response. The VIIRS TEB are calibrated with an on-board black body (BB) [13]. The DNB is also calibrated with the on-board SD [14]. Figure 1 is a schematic diagram for VIIRS and its on-board calibrators [15]. VIIRS

views the SV, earth view (EV), BB, and SD, respectively, via a rotating telescope assembly (RTA) and half angle mirror (HAM). Figure 2 shows the scan angles as well as the angle of incidence (AOI) for each view [15]. SNPP VIIRS covers almost the entire Earth surface every day and collects visible and infrared imagery and radiometric measurements of the land, atmosphere, cryosphere, and oceans.

In this paper we focus on the VIIRS RSB calibration. For VIIRS, the AOI of the SD exactly coincides with that of the SV as illustrated in Fig. 2. This is a design change over its predecessor, the Moderate Resolution Imaging Spectroradiometer (MODIS) [16, 17] which has SD and SV at different AOIs. So for VIIRS, the SD/SDSM calibration and the lunar calibration should in principle provide the same on-orbit changes over time of the calibration coefficients for the VIIRS RSB. With carefully derived input ingredients, we have shown in a preceding analysis that the SDSM is a superb monitor of the SD performance [8] and that SD calibration can provide stable and clean calibration coefficients, called SD F-factors, for the RSB [5]. However, a key assumption in the SD/SDSM calibration methodology that the SD degradation in the outgoing direction towards the SDSM can be used interchangeably with the outgoing direction towards the RTA, a part of the so called "degradation uniformity condition", has been found to be untrue. Throughout this paper we will refer to "degradation non-uniformity" to describe the general and non-trivial change in the relative angular dependence in the degradation of SD that contributes to the absolute anisotropy of the SD bidirectional reflectance distribution function (BRDF).

The degradation non-uniformity effect is especially pronounced for short wavelength bands [5, 8]. Consequently, a long-term bias may propagate into the derived calibration coefficients. In this paper, it will be shown that with careful correction of the view geometric effect, the lunar calibration can provide stable and clean calibration coefficients, to be referred to as the lunar F-factors in this paper for clarity, for the RSB. In general, the lunar F-factors are consistent with the SD F-factors, but band- and time-dependent differences between the two sets of F-factors can clearly be seen. Considering the potential bias of the SD F-factors due to the temporal non-

uniformity of the SD degradation, which is a primary but not necessarily the only reason for the differences of the two sets of F-factors, and the stability of the lunar surface's reflectance, the lunar calibration should provide the more reliable long-term calibration baseline. Nevertheless, the monthly lunar observations are infrequent and unavailable for several months out of the year due to a spacecraft roll angle safety constraint preventing a lunar view through the space view port [9-11]. Thus, an appropriate combination of the SD-based and lunar-based calibration coefficients, referred to as *hybrid calibration coefficients*, is the highlight of this work leading to an overall stable short- and long-term calibrated VIIRS RSB sensor data records (SDR). This is especially important for VIIRS ocean color environmental data records (EDR).

The ocean color EDR products [20-24] are highly sensitive to the accuracy of the RSB calibration, especially for the visible (VIS) and near-infrared (NIR) bands (M1-M7) that range from 410 to 862 nm from which VIIRS ocean color EDR products [25] are made. On the other hand, the ocean color EDR products, being highly sensitive to the accuracy of the calibration, are also where calibration accuracy can be checked. Significant long-term drifts have indeed been discovered in the VIIRS normalized water-leaving radiances from the short wavelength bands and the VIIRS chlorophyll calculated using the NOAA Interface Data Processing Segment (IDPS) SDR [19]. These are among the current official SDR products that use the SD F-factors derived by the VIIRS SDR team and that exhibit unexpected features due to the artificial seasonal oscillations and other inaccuracies in the SD F-factors [4]. The application of the reprocessed SDR with our best and latest improved SD F-factors does significantly improve the quality of the ocean color EDR products due to removal of the seasonal oscillations and other errors found in the SD calibration coefficients, but still fails to address the long-term drifts present in the products. The removal of the long-term drifts is finally made successful because of the application of the hybrid F-factors. A preliminary result of both our hybrid approach and the performance of the ocean color EDR with the hybrid F-factors implemented SDR have been briefly reported [18, 19]. The NASA Ocean Biology Processing Group (OBPG) has also reported their effort on this front [4]. The hybrid scheme is the final work in the long chain of

investigative efforts on VIIRS RSB calibration that include bi-directional reflectance factor (BRF), the vignetting function (VF), the degradation factor of the SD (H-factors), and the RSB calibration coefficients basing solely on SD, or the F-factors [5, 8, 28]. While F-factors from the SD should in principle be the final output of the calibration pipeline by design, due to the deviation propagated by the non-uniform degradation effect in the SD previously emphasized, this extended work is necessary to repair and to restore the core calibration pipeline. There remain additional key issues, including on-orbit change of the response-versus-scan angle (RVS) [27] and the impact of the on-orbit change of the relative spectral response (RSR) [5, 28] on EV radiance that need to be investigated.

In this paper we report on a timely update of the current progress in the calibration of the VIIRS RSB. The algorithms of the SDSM, SD, and lunar calibrations are briefly reviewed and the results of the calibrations are shown. The methodology to derive the hybrid calibration coefficients from the SD and lunar F-factors is described and reviewed in detail, and performance of the reprocessed ocean color EDR is demonstrated. This work completes the standard core of the methodology and analyses, and enables VIIRS to further many science products to reach higher data quality, especially for ocean color products.

2. SDSM Calibration

A. Algorithms

The SDSM calibration in this paper refers to the measurement of the SD reflectance performance by the SDSM during specially planned instrument operations. Figure 3 is a schematic diagram for the SD and SDSM calibration. The SNPP VIIRS SDSM shown in Fig. 3 is a ratioing radiometer consisting of a spherical integrating source (SIS) with a single input aperture and eight filtered detectors. The center wavelengths of the eight SDSM detectors are listed in Table 1. The SDSM views the SD, Sun, and the dark scene inside the SDSM alternately by changing the position of a fold mirror in front of the input aperture of the SIS. The screens in the front of the SD port and the sun-view port, as shown in Fig. 3, reduce the intensity of the

sunlight to prevent the saturation of the SDSM detectors for both the SD view and the direct sun views, respectively. The dark scene response provides the background response of the SDSM. In the SDSM calibration methodology, a linear approximation is applied to establish the relationship between the radiance of the incident sunlight at the center wavelength of a SDSM detector and the background-subtracted digital count dc_D reading from the detector [8]. Both the SD through the SD port and the SDSM entrance aperture through the SD sun-view port are fully illuminated during a short window of time when the satellite approaches the South Pole from the night side of the Earth. Only the SDSM responses to the SD with the view spot being fully illuminated and those to the sun view with the SDSM aperture also being fully illuminated can be used to derive the SD degradation.

The SD degradation at the center wavelength, λ_D, of the SDSM detector D can be tracked by its ratio of the SD view response to its sun-view response [8], i.e.,

$$H(\lambda_D) = \left\langle \frac{dc_{SD,D}}{\rho_{SD,SDSM}(\lambda_D)\tau_{SDS}\cos(\theta_{SD})} \right\rangle_{Scan,Sample} \Bigg/ \left\langle \frac{dc_{SV,D}}{\tau_{SVS}} \right\rangle_{Scan,Sample}$$

where $dc_{SD,D}$ and $dc_{SV,D}$ are background-subtracted SD and SV view responses of the SDSM detector D, respectively, $\rho_{SD,SDSM}(\lambda_D)$ is the BRF of SD with outgoing direction toward the SDSM at the time the instrument was launched, τ_{SDS} and τ_{SVS} are the VF of the SD port screen and SDSM sun-view port screen, respectively. θ_{SD} is the solar-zenith angle to the SD and $\langle\ldots\rangle_{Scan,Sample}$ indicates the average over the selected scans from the full illumination time period, which is called the "sweet spot", and samples in each scan. Due to design imperfection, the full illumination regions for the two views are not coincident [8]. As an improvement in the procedure, two independent and different "sweet spots" are selected for the SD view and the sun view, which are solar declination angle in the instrument coordinate system within the range of 13^o to 17^o for the SD view and solar elevation angle in the SDSM sun view port screen coordinate system within the range of -2^o to 2^o for the SDSM sun view, respectively [8].

Another improvement in the procedure is to first average the solar angle effect corrected SD view response and sun-view response over the selected scans separately prior to taking the ratio of the two [8]. This procedure differs from those used in other work and the one prescribed by the ATBD [15], but produces more robust results with less random noise in the derived H-factors. The BRF and the VFs, once correctly derived and implemented, should remove the dependence of $dc_{SD,D}$ on the solar angles in Eq. (1). All the BRF and VFs were measured prelaunch [26] and validated using the on-orbit measurements from the planned yaw maneuvers [27]. We have carefully re-derived these functions using the on-orbit yaw measurements [28] and our newly derived and much improved BRF and VFs are applied in this analysis. For the SDSM on-orbit degradation, the derived H-factors from the measurements of each SDSM detector are normalized at the time of launch [8].

B. SD Degradation

VIIRS SDSM calibration was performed for every orbit, generating about 14 events every day in the first few months on orbit, then the operational rate was reduced to once per day, and further reduced to once every two days after May 16, 2014. So far, more than 1200 SDSM measurements have been taken for VIIRS. The SDSM operational rate may be reduced again in the future to prolong the SDSM lifetime. In fact, the SDSM measurements for both Terra and Aqua MODIS have been performed with a lower frequency since their launches, currently once every 3 weeks for both Terra and Aqua MODIS [31].

The on-orbit SD degradation derived from the SDSM measurements via Eq. (1) at the wavelengths of the SDSM detectors is shown in Fig. 4 as symbols. The first set of SDSM measurements was made on November 8, 2011 when the SNPP VIIRS was turned on after 11 days on orbit. The nadir door was opened on November 21, 2011. The plot demonstrates that the SD started to degrade before the opening of the nadir door due to solar illumination through the SD port. It is also seen that the SD degraded much faster after the opening of the nadir door [8] due to extra exposure to the scattered sunlight from the earth scenes and also the increase of

the contaminants. An unexpected result emerged on February 5, 2014, on day 830, when the SD reflectance started to increase for about the next 75 days before reverting back. Furthermore, the subsequent trend does not return to the previously declining pattern expected. The reflectance also started to increase again a year later, suggesting a new seasonal repeating pattern in the SD. The effect is considered to be a real SD reflectance change as indicated by the results in the calculated RSB calibration coefficients, the F-factors, using the SD calibration, and is also confirmed to be a real reflectance change from the VIIRS ocean color products. As mentioned in our previous work [8], this short but dominating behavior is not previously observed form other satellite remote sensors and signals a different physical or chemical phenomenon of the SD surface not yet known.

The SD degrades faster at lower wavelengths as expected. In the past three and half years since VIIRS first light, the SD has degraded about 29.6%, 22.5%, 17.8%, 11.4%, 4.8%, 3.2%, 1.7%, and 1.2% at wavelengths of 412, 450, 488, 555, 672, 746, 865, and 935 nm, respectively. The measured SD degradations by the SDSM detectors change smoothly over time, although SDSM detectors D7 and D8 show more noise [8]. To reduce the noise, we fit the SD degradations measured by SDSM detectors D7 and D8 to exponential functions of time. The fitted SD degradations for the two wavelengths are displayed in Fig. 4 as solid lines. For other wavelengths, the measured SD degradations are used directly in this analysis considering both their smooth behavior with time and the difficulties in accurately simulating the unexpected behavior using analytical functions. The solid lines for detectors D1 to D6 in Fig. 4 are the linear connections of the measured SD degradations. The measured SD degradations prior to the opening of the nadir door are fitted to exponential functions, and the SD degradations for each wavelength, both symbols and the corresponding solid line, are normalized by the fitted value at the time of launch, i.e., October 28, 2011. Both the symbols and solid lines presented by the symbols in Fig. 4 are normalized values. The SD degradation is derived from the SDSM calibration at only 8 discrete wavelengths and value at any other wavelength within the spectral coverage is linearly interpolated. The SD degradation for the shortwave infrared (SWIR) bands

or wavelength longer than 935 nm is beyond the spectral coverage of the SDSM as seen in Table 1, and typically is assumed to be null at wavelengths longer than 935 nm.

The measured SD degradation results shown in Fig. 4 as symbols are much more stable and less noisy compared to those reported in literature [6, 7]. As previously stated, several key new improvements are used for this analysis: better selection of the "sweet spots", carefully re-derived BRF for the SD, VF for the SD screen, and VF for the SDSM sun-view screen, and finally, improved numerical treatments [8]. The results in Fig. 4 demonstrate that the SD degradation can be accurately tracked by the SDSM calibration, whether or not the change is expected, and for a multi-year trend or sudden changes alike. In principle, it catches the SD degradation for the outgoing direction toward the SDSM view direction. With the assumption that the SD degrades uniformly with respect to the incident and outgoing directions, the SD degradation derived from the SDSM calibration can be applied following the standard SD calibration methodology to derive the RSB calibration coefficients. However, it has been demonstrated in our previous works that the uniformity assumption of the SD degradation is not entirely valid and the discrepancy may induce long-term bias in the RSB calibration coefficients and VIIRS EV radiance, especially at shorter wavelengths [8]. It is also estimated that the SD degradation beyond 935 nm may not be negligible as assumed when the instrument was designed [8]. The former will be discussed in latter sections, while the later will be discussed in a separate work.

3. SD Calibration

A. Algorithms

The SD calibration in this paper refers to the measurement of the RSB performance using the SD as a reflectance reference. The VIIRS SD is made of Spectralon® and is installed inside the VIIRS instrument. The screen in the front of the SD port, as shown in Fig. 3, reduces the intensity of the sunlight to prevent saturation of the RSB as well as the SDSM detectors, as mentioned previously. The center wavelengths of the RSB are listed in Table 1. For VIIRS

RSB, the background response is provided by the detector reading of the SV. In the VIIRS RSB radiance retrieval methodology, a quadratic approximation is applied to establish the relationship between the radiance of the incident sunlight at the center wavelength of a RSB detector and the background-subtracted digital number *dn* of the detector. In the SD calibration calculation, only the RSB responses to the SD with the view spot being fully illuminated, during the short window of time when the satellite crosses the terminator from the night side to the dayside of the Earth, can be used to derive the RSB calibration coefficients, F-factors. This proper range corresponds to the same "sweet spot" previously discussed for SDSM SD view.

The RSB calibration coefficients, or the F-factors, using the SD observation can be calculated by [5]

$$F(B,D,M,G,t) = \left\langle \frac{RVS(\vartheta_{SD},B)\int RSR_B(\lambda,t)\cdot L_{SD}(\lambda)d\lambda}{\left[\sum_{j=0}^{2} c_j(B,D,M,G)dn_B^j(Sample,Scan,D)\right]\int RSR_B(\lambda,t)d\lambda} \right\rangle_{Scan,Sample}$$

where *B*, *D*, *M*, and *G* are band number, detector number, mirror side of the HAM and gain status of the band, respectively. $RVS_{B,SD}$ is the response versus scan angle (RVS) at the AOI of the SD for band B and RSR_B is the RSR of the band. $c_0(B,D,M,G)$, $c_1(B,D,M,G)$, and $c_2(B,D,M,G)$ are temperature effect corrected prelaunch calibration coefficients, *dn* is the background-subtracted instrument response of band *B* and detector *D* during the SD view, and $\langle\ldots\rangle_{Scan,Sample}$ indicates the average over the selected scans of the "sweet spot" and samples in each scan. It should be clarified that the refitted prelaunch coefficients with all offset coefficients set to zero are ones used in this analysis. In Eq. (2), $L_{SD}(\lambda)$ is the radiance of the sunlight reflected by the SD and can be expressed as

$$L_{SD}(\lambda) = I_{Sun}(\lambda)\cdot\tau_{SDS}\cdot\cos(\theta_{SD})\cdot BRF_{RTA}\cdot h(\lambda)/d_{VS}^2, \quad (3)$$

where I_{Sun} is solar irradiance, BRF_{RTA} is the BRF for the outgoing direction of the RTA through which the RSB views the EV, SV, SD, and other on-board calibrators. $h(\lambda)$ is the on-orbit SD degradation tracked by the SDSM and is normalized to October 28, 2011, and d_{VS} is the VIIRS-Sun distance. The dependence of the reflected solar radiance on the solar angles is accounted for by BRF, VF, and $\cos(\theta_{SD})$. The BRF and VF were measured prelaunch [29] and validated on-orbit using the on-orbit measurements from the planned yaw maneuvers [30]. We have re-derived these functions carefully using the yaw measurements and the newly derived and much improved BRF and VF are used in this analysis as well as in preceding investigative efforts [26]. As mentioned in Section 2, the SD degradation, $h(\lambda)$, describes the SD degradation for the outgoing direction towards the SDSM view, but may differ from the actual degradation of the SD for the outgoing direction towards the RTA view, especially for shorter wavelength bands due to the non-uniformity effect in SD degradation [8]. The temporal non-uniformity of the SD degradation has been observed and confirmed in RSB observations [5] and its impact will be discussed further in later sections. As also mentioned in the previous section, the SDSM is not capable of catching SD degradation beyond the 935 nm spectral region [8], and thus the calibration coefficients derived from the SD calibration using Eq. (2) may include additional errors due to this missing information. The missing spectral coverage in the NIR region will be investigated further in a separate work.

B. SD Calibration Coefficients

VIIRS SD calibration is performed in every orbit, generating about 14 SD calibration events daily, and thus 14 sets of RSB calibration coefficients can be derived daily. Figure 5 shows the calibration coefficients, or SD F-factors, derived from the SD calibration for VIIRS band M1. Compared to those reported by others [3, 4], the F-factors in Fig. 5 have no sudden or random jumps. The seasonal oscillations seen in literature [3, 4] have either been greatly reduced or completely removed but small random fluctuations on the level of ~0.1% remain in the F-factors. Considering that the specification for the RSB calibration is 2% and that the expectation for the stability of the F-factors from the ocean color applications is about 0.1%, which is a much higher

requirement for the accuracy of the RSB calibration than those in other science disciplines [20-25], the new F-factors derived from the SD calibration with improved BRF, VF, and SD degradation are very clean and of considerably high quality.

The band-averaged SD F-factors for the VIS and NIR bands are displayed in Fig. 6. They are normalized to the time of the first measurement. The F-factors are strongly wavelength dependent and increase with time. As the gain is inversely proportional to the F-factor, it means that the instrument performance is decreasing over time. The largest increase in F-factor occurs at the NIR bands I2 and M7, both at the same wavelength of 862 nm, while the degradations of the short wavelength bands are much smaller. This result contrasts from MODIS RSB for which the largest degradation occurs at short wavelength bands [16, 32]. The F-factors of VIIRS bands I2 and M7 have increased 54%, equivalent to a gain degradation of 35% since launch on October 28, 2011, while the increases for bands M1, M2, and M3 are less than 2% with band M3 having the smallest increase. From the results in Fig. 6, it is seen that the NIR bands have larger gain degradations, corresponding to larger increases of the F-factors. The larger gain degradations of the VIIRS NIR RSB are mainly due to the degradation of the RTA [33-35]. The other major gain degradation mechanism is that of the HAM, which degrades more at short wavelengths and results in the largest degradation in band M1 and among short wavelength bands M1-M3 [5]. Since there is a RTA in front of the VIIRS scan mirror (the HAM), it has degraded much less in comparison to the scan mirror of either MODIS instrument [16, 32]. Thus, the VIIRS short wavelength bands have much less degradation in the past three and half years than either Terra or Aqua MODIS in their initial three and half years on-orbit. The MODIS RSB degradations are mainly due to the degradation of the scan mirror and thus degrade faster at short wavelength bands [16, 32]. Also, as it has been stated, the calibration coefficients for the short wavelength bands and SWIR bands have non-negligible errors due to the non-uniformity of the SD degradation and from the incapability of the SDSM calibration for the SWIR spectral range.

4. Lunar Calibration

A. Lunar Calibration Algorithms

VIIRS views the Moon from the SV port that has the same AOI as the SD although two optical paths on the HAM are the reverse of each other. The Moon, being a well-studied target with a very stable reflectance in the VIS and NIR spectral regions [36], has been widely used to track the RSB on-orbit gain changes [37, 38]. For VIIRS it can then be used to track the RSB gain change at the SD AOI to provide direct comparison without an RVS issue, and in addition, as we will show later, to restore calibration accuracy. With the approximation that the difference between the detector on-orbit changes is negligible, the detector averaged lunar F-factor can be expressed as [10, 11]

$$F(B,D,M,G,t) = \frac{g(B)N_M}{\sum_{D,P,S} L_{pl}(B,D,P,S)\delta(M,M_S)} \quad (4)$$

where $g(B)$ corrects the relative geometric effects for band B, N_M is the number of scans, with HAM side M. In the summation, S is scan number, P is pixel number along the scan direction, $L_{pl}(B,D,P,S)$ is the lunar irradiance calculated using the prelaunch calibration coefficients, and M_S is the mirror side for the scan S. Our analysis uses the four scans around the center of the lunar observation, during which the instrument scans the center of the lunar surface, to calculate the relative F-factor for each lunar calibration, two for each mirror side. $g(B)$ depends on the lunar view geometry, which is described by Sun-Earth distance, sensor-Moon distance, lunar phase angle, and lunar librations. The Robotic Lunar Observatory (ROLO) model [39] can provide the predicted lunar irradiance, which can be used as $g(B)$ to account for the geometric effect in Eq. (4). The absolute uncertainty of the ROLO model can be as large as ~5% for short-wavelength bands and the uncertainty is even larger for the NIR bands. However, the relative uncertainty of the irradiance predicted by the ROLO model over the entire view geometry is about 1% [40]. Since the lunar phase angle is confined to a selected and more restricted region that has been carefully studied [9], the relative uncertainty of the lunar irradiance predicted by the ROLO model for VIIRS scheduled lunar observations should be smaller than ~1%. Thus, the

lunar calibration may not provide accurate absolute F-factors for VIIRS RSB, but it can provide relative F-factors or the on-orbit gain change within ~1% accuracy. To distinguish the F-factor derived from the SD/SDSM calibration, the relative F-factors obtained from the lunar calibration will be clarified as lunar F-factors.

The lunar irradiance is strongly dependent on viewing geometry. To reduce the potential error in the correction of the lunar viewing geometry, the lunar observations are planned to be as geometrically identical to each other as possible. Thus, the scheduled VIIRS lunar observations are carefully planned and selected, as are MODIS scheduled lunar observations [9]. The main parameters used to select the lunar observations are lunar phase angle defined as the angle formed by the Sun, the Moon, and the sensor, as well as the roll angle. The former is limited to a small range to keep the geometric effect correction as small as possible, while the latter is kept as small as possible to minimize instrument and spacecraft safety concerns. For the VIIRS scheduled lunar observations, the acceptable phase angle range was originally chosen as [–55.5^o, –54.5^o], where the phase angle is defined to be negative for a waxing Moon and positive for a waning Moon [9]. Later, the range was changed to [–51.5^o, –50.5^o] to minimize the roll angles required for the scheduled lunar observations [10, 11].

B. Lunar Calibration Coefficients

The F-factors, derived for SNPP VIIRS VIS and NIR bands from the scheduled lunar observations, are shown in Fig. 7 as symbols. Every year there are about nine months during which the SNPP VIIRS can observe the Moon within the acceptable phase angle range with roll maneuvers [10, 11]. In the other three months or so, the Moon cannot be observed even with roll maneuvers since the roll angle is restricted to be within the range of [–14^o, 0^o]. Before April 2012, the SNPP VIIRS lunar observation data were taken in the SV sector. Since co-registration is not applied to the SV sector, some of the RSB may see a partial moon during a lunar calibration through the SV and such a lunar calibration cannot be used to track the gain change for all RSB [10, 11]. Thus, in this analysis the VIIRS lunar observations before April 2012 are

excluded. To resolve this issue, a sector rotation has been implemented in every scheduled lunar observation since April 2012 [10, 11]. Similar to SD F-factors, the lunar F-factors are strongly wavelength dependent and increase with time [5]. As expected, the largest increase occurs in the F-factors for bands I2 and M7, and changes in those for short wavelength bands are small. Among the three shortest wavelength bands M1-M3, band M1 has the largest increase in the last three and half years in the lunar F-factors. The two main competing mechanisms, as discussed earlier, one due to the degradation of the RTA and the other due to the HAM degradation, are also clearly seen in the lunar F-factors as in the SD F-factors [5]. Compared to those reported in literature [10, 11], the lunar F-factors in Fig. 8 are much more smooth and less noisy. Seasonal oscillations with amplitudes of about 0.5% were clearly seen in the lunar F-factors reported in literature [10, 11], and it is believed that the oscillations were due to the uncertainty of the ROLO model [12]. Any relative errors of the ROLO model or any other lunar model can induce such seasonal oscillations and, in fact, the oscillations are within the relative uncertainty of the ROLO model [40]. In this analysis, we have introduced a correction based on the viewing geometry to remove the oscillation pattern, and the correction has been applied in the lunar F-factors displayed in Fig. 8. The detail of the correction will be discussed in a separate work.

C. Lunar and SD result discrepancy

The SD F-factors are also drawn in Fig. 7 for VIS and NIR bands with solid lines for comparison. The lunar F-factors are normalized to the SD F-factors corresponding to the April 2012 lunar observation. It can be seen that the F-factors from the two calibrations are in general agreement but with observable differences. The differences between the two sets of F-factors also increase with time. For a more clear demonstration of the differences, Fig. 8 only shows the F-factors for bands M1-M4. Among the four bands, the largest difference occurs in the band M4, which is about 1.3%, and the band M2 has the second largest difference, which is about 1.0%. The differences for bands M1 and M2 are about 0.6% and 0.7%, respectively. The exact root causes of the differences between the SD/SDSM calibration and the lunar calibration are difficult to identify. However, in our previous works using both SDSM and RSB measurements

from SD observations, it has been demonstrated that the SD degrades non-uniformly with respect to incident direction, especially for short wavelength bands [5, 8].

Figure 9 shows an evolution of the incident angle dependency that demonstrates increasing non-uniformity of the SD reflectance property for both the SDSM view and the RSB view from SDSM and RSB measurements, respectively. The slope in the plot indicates, for each calibration event shown, the dependency of the H-factor or the F-factor with respect to solar declination angle in the instrument coordinate system. If the SD degrades uniformly with respect to the incident angle, then the slope will be zero instead. For D1-D4 and M1-M4, however, the slopes grow with time as degradation and the associated non-uniformity worsens, while for other SDSM detectors and RSB the slopes are close to zero. The different signs of the slopes for SDSM detectors and RSB bands, the two being at different outgoing angles with respect to the SD, indicate that the SD also degrades non-uniformly with respect to the outgoing direction. Figure 9 demonstrates that the SD degradation uniformity assumption used in SD/SDSM calibration methodology does not hold and invalidates the use of the SD degradation factor at the outgoing angle toward the RSB being replaced by the SD degradation factor at the different outgoing angle measured by the SDSM. The lunar calibration based on irradiance, however, faces no degradation issue and in principle should provide more reliable and accurate long-term RSB gain on-orbit changes. Thus, the non-uniformity of the SD degradation should be one of the main reasons for the discrepancy of the two sets of the F-factors and should be the primary one for short wavelength bands.

5. Hybrid Approach

Although lunar calibration can provide more accurate and reliable long-term VIIRS RSB on-orbit gain changes, lunar observations can only be scheduled for about nine times a year given phase angle and roll maneuver constraints [10, 11]. The lunar calibration results also have greater measurement uncertainty due to difficulty in making an accurate correction for the viewing geometry effect on the lunar irradiance. Meanwhile, the SD/SDSM calibration can

provide VIIRS RSB on-orbit change for each orbit. The derived F-factors may not be accurate in the long-term but are smooth and stable in the shorter time frame to complement lunar-based results. A viable workaround is to use the lunar F-factors as the long-term baseline and the SD F-factors for short-term gain variation.

In the current procedure, the gain status of the dual gain bands is fixed at high gain during a scheduled lunar observation [10, 11]. Then the ratio of the lunar factors and the SD F-factors can be calculated for single gain bands or dual gain bands with high gain status by

$$R(B,t) = f(B,M,t)/\langle F(B,D,M,0,t)\rangle_{D,t-15<t_i<t+15,M}, \quad (5)$$

where $<\ldots>_{D,t-15<t_i<t+15,M}$ indicates the average over detectors and the time period of 30 days centered at time t where lunar observation is implemented and M stands for HAM sides. The difference between the lunar and the SD F-factors is mainly due to the inaccuracy of the SD degradation used for the RSB view and does not pertain to gain status, the ratio derived from the measurements with high gain status can be applied for low gain status of the dual gain bands. To reduce the random noise and to get the ratios at any given time, we fit the ratios of each band to an exponential function of time, that is,

$$r(B,t) = \exp(c_0(B) + c_1(B)t + c_2(B)t^2), \quad (6)$$

where c_0, c_1 and c_2 are coefficients of the quadratic form. Figure 10 shows the band-averaged ratios of the two sets of F-factors and fitted functions for VIS and NIR bands, where symbols are the measured ratios and solid lines are fitted functions. It is clearly shown that the ratios are band dependent and increase with time. The non-negligible differences between the SD and lunar F-factors for short wavelength bands are as expected according to the non-uniformity degradation of the SD. It is also noticeable that there are non-negligible differences between the two sets of F-factors for other bands with longer wavelengths. This indicates additional and unknown mechanisms contributing to the differences of the F-factors besides the non-uniformity of the SD degradation. It is also worth noting that the ratios can be approximately classified into two groups, with bands M3, M4, and I1 as one group with larger ratios and the remaining bands

as another. The fitted smooth functions are normalized at the time of the first lunar observation, April 2012, used in this analysis. With the normalized fitted smooth functions, we can construct a set of hybrid F-factors by

$$\mathcal{F}(B,D,H,G) = r(B,t)\cdot F(B,D,H,G)\,. \qquad (7)$$

With Eq. (7), a set of hybrid calibration coefficients can be generated. Effectively, the SD F-factor is corrected by a smooth but time-dependent scaling dictated by the long-term lunar results. The new set averts the errors of the SD F-factors due to the SD degradation non-uniformity effect and other unknown reasons, but keeps the frequency and smoothness of the SD F-factors. This is a different approach from that described in reference [12] where the SD and lunar F-factors are fitted to a linear function of time and the fitted linear function is used to adjust the SD F-factors.

This is, in principle, applicable to all bands, but we focus the application to M1-M4 only because these are the primary ocean color bands and are certain of being affected by the non-uniformity effect of the SD degradation. Figure 11 shows both the hybrid F-factors and the SD F-factors for the band M1. As expected, the hybrid F-factors are larger than the SD F-factors and the differences between the two sets of F-factors increase with time. It is also noticeable that the hybrid F-factors look smoother with time, considering the increasing rates, than the SD F-factors. Figures 12 and 13 show the hybrid F-factors and the SD F-factors for the VIIRS band M2 and M4, respectively. Same for the band M1, the hybrid F-factors look more smooth and reasonable. Figure 14 displays the band averaged hybrid F-factors and SD F-factors. As expected, the differences between the two sets of F-factors for the band M4 are larger than those for the other three bands. The hybrid approach is not applied to the time period before April 2012 due to the inaccuracy of the lunar F-factors induced by the partially observations of the lunar surface [10, 11].

6. SDR and Ocean Color EDR Products

In VIIRS SDR products, the F-factor is the key input for the at-aperture radiance *L*, observed by detector *D* of band *B* at pixel *P* of scan *S* with HAM side *M* at time *t*, which is calculated by the following [1, 2]:

$$L_B(P,S,D,t) = \frac{F(B,D,M,G,t)\sum_{j=0}^{2} c_j(B,D,M,G)dn_B^j(P,S,D)}{RVS(\vartheta,B)} \quad (8)$$

where $RVS(\vartheta,B)$ is the RVS at the AOI, ϑ, of the HAM and $c_0(B,D,M,G)$, $c_1(B,D,M,G)$, and $c_2(B,D,M,G)$ are the temperature-effect-corrected prelaunch measured offset, linear, and nonlinear coefficients of the quadratic form [14]. The prelaunch measured calibration coefficients were refitted later with the offset set to zero. $F(B,D,M,G,t)$ is the time-dependent F-factor. The RVS was measured prelaunch [41] but may change on-orbit due to the degradation of the scan mirror as demonstrated by both Aqua and Terra MODIS scan mirrors [27]. Since the HAM is inside of the instrument, it degrades much more slowly than the scan mirrors of the two MODIS instruments [5]. The slower degradation of the VIIRS HAM can be seen from the much slower degradation of the VIIRS short wavelength VIS bands. The HAM degradation is not considered in this paper and is beyond the scope of this work. The current official SDR products are produced by the NOAA IDPS using the F-factors derived from the SD/SDSM calibration [25]. The VIIRS Ocean Color EDR Team at the NOAA Center for Satellite Applications and Research (STAR) has reprocessed the SDR using the Algorithm Development Library (ADL) with the improved SD F-factors for selected targets and also reprocessed the SDR with the hybrid F-factors for the entire mission. The reprocess of SDR using the ADL is a time consuming process but a robust ratio approach, recently developed by the authors, has dramatically improved the efficiency by two orders of magnitude [42].

The NOAA Ocean Color team has developed a global near-real-time VIIRS ocean color data processing system, which automatically downloads global VIIRS Raw Data Records (RDR or Level-0 data), Sensor Data Records (SDR or Level-1B data), and ancillary data in near real-time, and then processes them into ocean color EDR (Level-2) data [19]. The NOAA Multi-

Sensor Level-1 to Level-2 (NOAA-MSL12) software package is used for VIIRS ocean color SDR-to-EDR processing. MSL12 is an official NOAA VIIRS ocean color data processing system, and was originally developed for the purpose of using a consistent data processing system to produce ocean color data from multiple satellite ocean color sensors [25, 43-45]. The global Level-3 binned products (daily, 8-day, monthly, and climatology) are also generated routinely for evaluation [19, 25]. The VIIRS ocean color team has been routinely processing and evaluating VIIRS ocean color products from the start of the VIIRS mission using the IDPS SDR products. They have also reprocessed ocean color EDR using the SDR processed with the improved SD F-factors and the hybrid F-factors described in this analysis.

The preliminary evaluation of the reprocessed ocean color EDR using the SDR generated with the hybrid F-factors has been reported in our previous papers [18, 19]. Here we briefly show the improvements of the further updated hybrid F-factors on the VIIRS ocean color products. The detailed evaluation of the improvements of new hybrid LUTs on the ocean color products, as well as the improvements of the ocean color algorithms, will be discussed elsewhere. We also plan to use the hybrid F-factors for forward daily processing very soon, utilizing the previously mentioned ratio-approach method [42].

Figures 15 and 16 show the time series of VIIRS-derived $nL_w(\lambda)$, normalized water-leaving radiance, at wavelengths of 443 (M2) and 551 nm (M4), respectively, over the Hawaii region (oligotrophic waters). $nL_w(\lambda)$ spectra derived with the IDPS SDR processed with standard operational F-factors are represented by solid diamonds. The $nL_w(\lambda)$ derived using the SDR reprocessed with our new hybrid F-factors at the two wavelengths are shown by solid squares. The two figures show that $nL_w(\lambda)$ data derived with the IDPS SDR have a large anomaly before April 20, 2012 and a long-term drift for both bands. The newly derived $nL_w(\lambda)$ spectra with the hybrid F-factors are much improved and the long-term drifts are significantly reduced. This is also true for 410 nm (M1) and 488 nm (M3), which are not shown. The trend from the Marine Optical Buoy (MOBY) data, the direct in-situ measurements of $nL_w(\lambda)$ using a system of buoys [47, 48], is shown in Figs. 15 and 16 (in solid triangles). The comparison with the MOBY result

further confirms that the SDR using hybrid F-factors significantly elevates the accuracy of the ocean color products. Figure 17 shows VIIRS Chl-a derived from the newly reprocessed SDR with the hybrid F-factors and IDPS SDR in the same region. Chl-a data based on IDPS SDR (solid diamonds) show a clear long-term drift of about 15%, while the new Chl-a results show clear reduced long-term trend (solid squares).

It should be pointed out that the long-term drifts observed in ocean color EDR generated with the IDPS SDR cannot be removed by the SDR produced with our improved SD F-factors, although the quality of the products are improved due to the removal of the seasonal oscillations and other errors in the F-factors used to derive the IDPS SDR. Also, the ratios of the lunar F-factors and SD F-factors for bands M2 and M4 are quite different, as demonstrated in Fig. 10 and as described in the above section. In fact, the long-term drifts in the $nL_w(\lambda)$ products produced with the IDPS SDR are indeed band dependent and quite different for bands M2 and M4 as demonstrated in Figs. 15 and 16, and the above mentioned difference between M2 and M4 F-factor-ratios in the hybrid approach provides the correct remedy for the removal of the long-term drift in each band. Furthermore, this difference in the F-factor ratios is the required element in reducing the long-term drift in the Chl-a product since Chl-a strongly depends on the $nL_w(\lambda)$ radiance ratio (differences) of the two bands. Without this difference, the long-term drifts in the Chl-a data cannot be removed. This is slightly different from the work in reference [12] where SD F-factor and lunar F-factor differences are similar for all bands, and this seems unable to explain the removal of the long-term drifts. Additionally, the long-term drifts in both ocean color products derived from the IDPS SDR are downward, while the hybrid F-factors induce upward long-term corrections in $nL_w(\lambda)$ for all wavelength and in the Chl-a product. Our corrected product results are all upward for 410 nm, 443 nm, 486 nm and 551 nm, consistent with the ratio of the lunar F-factors over the SD F-factors inducing an upward direction. In reference [12], although the 410 nm and the 443 nm results are upward, their corrected 486 nm and 551 nm results do not tend upward as expected by their upward direction in correction.

7. Conclusions

We have completed the long chain of investigative efforts into the core calibration pipeline for VIIRS RSB. The overall improvement achieves an unprecedented degree of accuracy of the calibration coefficients, on the level of ~0.2% (with a confidence level of k=1), that helps the ocean color products meet very stringent requirements [46]. All required components of the calibration pipeline have been carefully examined and their characterization has been made robust. The BRF and VFs are correctly derived and implemented, the sweet spot selection is made proper and the SDSM correctly captures SD degradation. The degradation non-uniformity in the solar diffuser previously discovered for VIIRS, and also present for other sensors, has introduced errors into the final science products that are beyond the calibration capability of the old methodology based solely on the solar diffuser. The design change on VIIRS paves the way for the hybrid scheme using lunar based calibration to serve as the long-term calibration baseline, which in turn mitigates the SD performance issue and leads to new combined F-LUTs that generate the correct and best result. The updated results demonstrate that the calibration methodology is correct, but that previously unforeseen physical effects, including the degradation non-uniformity of the SD, can introduce unexpected deviations. Our investigative work and the subsequent improvements are successful in both keeping the core structure of the calibration algorithm intact and improving the quality of ocean color products. The extra insertion using the lunar result in the hybrid scheme is an effective but a simple modification that averts radical change to the calibration pipeline. The current work marks an important milestone in validating and improving the core calibration algorithms and the analysis procedures.

Acknowledgments

The work was supported by the Joint Polar Satellite System (JPSS) funding. We thank the MOBY team for providing the in situ data. We would like to thank Mike Chu for his continuing encouragement of high standards in research quality and scientific integrity. We would also like

to thank Jennifer Dodd for proofreading the manuscript and providing expert insights. The views, opinions, and findings contained in this paper are those of the authors and should not be construed as an official NOAA or U.S. Government position, policy, or decision.

References

1. C. Cao, F. Deluccia, X. Xiong, R. Wolfe, and F. Weng, "Early on-orbit performance of the Visible Infrared Imaging Radiometer Suite (VIIRS) onboard the Suomi National Polar-orbiting Partnership (S-NPP) satellite," IEEE Trans. Geosci. Remote Sens., 52, 1142–1156 (2014).
2. X. Xiong, J. Butler, K. Chiang, B. Efremova, J. Fulbright, N. Lei, J. McIntire, H. Oudrari, J. Sun, Z. Wang, and A. Wu, "VIIRS on-orbit calibration methodology and performance," J. Geophys. Res. Atmos., 119, 5065–5078 (2014).
3. N. Lei, Z. Wang, J. Fulbright, S. Lee, J. McIntire, K. Chiang, and X. Xiong, "Initial on-orbit radiometric calibration of the Suomi NPP VIIRS reflective solar bands," Proc. SPIE, 8510, 851018 (2012).
4. J. C. Cardema, K. Rausch, N. Lei, D. I. Moyer, and F. DeLuccia, "Operational calibration of VIIRS reflective solar band sensor data records," Proc. SPIE, 8510, 851019 (2012).
5. J. Sun and M. Wang, "On-orbit calibration of the Visible Infrared Imaging Radiometer Suite reflective solar bands and its challenges using a solar diffuser," Applied Optics, 54, 7210-7223 (2015).
6. E. Hass, D. Moyer, F. DeLuccia, K. Rausch, and J. Fulbright, "VIIRS solar diffuser bidirectional reflectance distribution function (BRDF) degradation factor operational trending and update," Proc. SPIE, 8510, 851016 (2012).
7. J. Fulbright, N. Lei, K. Chiang, and X. Xiong, "Characterization and performance of the Suomi-NPP VIIRS solar diffuser stability monitor," Proc. SPIE, 8510, 851015 (2014).
8. J. Sun and M. Wang, "Visible infrared image radiometer suite solar diffuser calibration and its challenges using solar diffuser stability monitor," Appl. Opt., 36, 8571-8584 (2014).

9. J. Sun and X. Xiong, "Solar and lunar observation planning for Earth-observing sensor", *Proc. SPIE,* 8176, 817610 (2011).
10. J. Sun, X. Xiong, and J. Butler, "NPP VIIRS on-orbit calibration and characterization using the Moon," *Proc. SPIE,* vol. vol. 8510, pp. 85101I (2012).
11. X. Xiong, J. Sun, J. Fulbright, Z. Wang, and J. Butler, "Lunar Calibration and Performance for S-NPP VIIRS Reflective Solar Bands", submitted to *IEEE Trans. Geosci. Remote Sensing.*
12. R. E. Eplee, Jr., K. R. Turpie, G. Meister,F. S. Patt, B. A. Franz, and S. W. Bailey, "On-orbit calibration of the Suomi National Polar-Orbiting Partnership Visible Infrared Imaging Radiometer Suite for ocean color applications," Applied Optics, 54, 1984-2006 (2015).
13. B. Efremova, J. McIntire, D. Moyer, A. Wu, and X. Xiong, "S-NPP VIIRS thermal emissive bands on-orbit calibration and performance," *J. Geophys. Res. Atmos.*, 119, 10859–10,875 (2014).
14. S. Lee, J. McIntire, H. Oudrari, T. Schwarting, X. Xiong, "A new method for suomi-NPP VIIRS on-orbit day night band radiometric calibration," IEEE Trans. Geosci. Remote Sens. 2013, 53, 324–334.
15. N. Baker, "Joint Polar Satellite System (JPSS) VIIRS radiometric calibration algorithm theoretical basis document (ATBD)," Goddard Space Flight Center, Greenbelt, Maryland, NASA, May 15, 2013.
16. X. Xiong, J. Sun, W. Barnes, V. Salomonson, J. Esposito, H. Erives, and B. Guenther, "Multiyear on-orbit calibration and performance of Terra MODIS reflective solar bands", *IEEE Trans. Geosci. Remote Sensing*, 45, 879-889 (2007).
17. J. Sun, X. Xiong, W. L. Barnes, and B. Guenther, "MODIS Reflective Solar Bands On-Orbit Lunar Calibration", *IEEE Trans. Geosci. Remote Sens*. 43, 2383-2393 (2007).
18. J. Sun and M. Wang, "VIIRS Reflective Solar Bands On-Orbit Calibration and Performance: A Three-Year Update," Proc. SPIE, 9264, 92640L (2014).

19. M. Wang, X. Liu, L. Jiang; S. Son; J. Sun; W. Shi; L. Tan; P. Naik, K. Mikelsons, X. Wang; V. Lance, “Evaluation of VIIRS ocean color products,” Proc. SPIE 9261, 92610E (2014).
20. H. R. Gordon, and M. Wang, “Retrieval of water-leaving radiance and aerosol optical thickness over the oceans with SeaWiFS: A preliminary algorithm,” Appl. Opt., 33, 443–452 (1994).
21. M. Wang, “Remote sensing of the ocean contributions from ultraviolet to near-infrared using the shortwave infrared bands: simulations,” Appl. Opt., 46, 1535–1547 (2007).
22. M. Wang and W. Shi, “The NIR-SWIR combined atmospheric correction approach for MODIS ocean color data processing,” *Opt. Express,* 15, 15722–15733, 2007.
23. M. Wang, J. Tang, and W. Shi, “MODIS-derived ocean color products along the China east coastal region,” *Geophys. Res. Lett.,* 34, L06611, http://dx.doi.org/10.1029/2006GL028599, 2007.
24. M. Wang, W. Shi, and J. Tang, “Water property monitoring and assessment for China’s inland Lake Taihu from MODIS-Aqua measurements,” *Remote Sens. Environ.,* 115, 841–845, 2011.
25. M. Wang, X. Liu, L. Tan, L. Jiang, S. Son, W. Shi, K. Rausch, and K. Voss, “Impact of VIIRS SDR performance on ocean color products,” J. Geophys. Res. Atmos., 118, 10347–10360 (2013).
26. J. Sun and M. Wang, “On-orbit characterization of the VIIRS solar diffuser and solar diffuser screen," Appl. Opt., 54, 236-252 (2015).
27. J. Sun, X. Xiong, A. Angal, H. Chen, A. Wu, and X. Geng, “Time dependent response versus scan angle for MODIS reflective solar bands,” *IEEE Trans. Geosci. Remote Sens.*, vol. 52, No. 6, 3159-3174, 2014.
28. N. Lei, B. Guenther; Z. Wang; X. Xiong, “Modeling SNPP VIIRS reflective solar bands optical throughput degradation and its impacts on the relative spectral response,” Proc. SPIE 8866, 88661H (2013).

29. JPSS, “Joint Polar Satellite System (JPSS) VIIRS Reflective Solar Bands - Performance Verification Report (PVR),” (NASA Goddard Space Flight Center, Greenbelt, MD, USA, 2011).
30. J. McIntire, D. Moyer, B. Efremova, H. Oudrari, X. Xiaoxiong, “On-Orbit Characterization of S-NPP VIIRS Transmission Functions”, *IEEE Trans. Geosci. Remote Sensing* 53, 2354 - 2365 (2015).
31. X. Xiong, A. Angal, J. Sun, J. Choi, and E. Johnson, "On-orbit performance of MODIS Solar Diffuser Stability Monitor", *Journal of Applied Remote Sensing*, 8, 083514-1-14 (2014).
32. X. Xiong, J. Sun, X. Xie, W. L. Barnes, and V. V. Salomonson, “On-orbit calibration and performance of Aqua MODIS reflective solar bands,” IEEE Trans. Geosci. Remote Sens., 48, 535–545 (2010).
33. F. De Luccia, D. Moyer, E. Johnson, K. Rausch, N. Lei, K. Chiang, X. Xiong, and J. Fulbright, E. Haas, G. Iona, “Discovery and characterization of on-orbit degradation of the Visible Infrared Imaging Radiometer Suite (VIIRS) Rotating Telescope Assembly (RTA),” Proc. SPIE, 8510, 85101A (2012).
34. J. D. Barrie, P. D. Fugua, M. J. Meshishnek, M. R. Ciofalo, C. T. Chu, J. A. Chaney, R. M. Moision, and L. Graziani, “Root cause determination of on-orbit degradation of the VIIRS rotating telescope assembly,” Proc. SPIE, 8510, 8510B (2012).
35. G. Iona, J. Butler, B. Guenther, L. Graziani, E. Johnson, B. Kenedy, C. Kent, R. Lambeck, E. Waluschka, X. Xiong, “VIIRS on-orbit optical anomaly – Investigation, analysis, root cause determination and lessons learned,” *Proc. SPIE*, 8510, 85101C (2014).
36. H.H. Kieffer, "Photometric Stability of the Lunar Surface", *Icarus* 130, 323-327 (1997).
37. R. A. Barnes, R.E. Eplee, Jr., F.S. Patt, and C.R. McClain, “Changes in the radiometric stability of SeaWiFS determined from lunar and solar measurements”, *Appl. Opt.*, 38, 4649-4664 (1999).

38. J. Sun, X. Xiong, W. L. Barnes, and B. Guenther, “MODIS Reflective Solar Bands On-Orbit Lunar Calibration”, *IEEE Trans. Geosci. Remote Sens*. 43, 2383-2393 (2007).
39. Hugh H. Kieffer and Thomas C. Stone, "The Spectral Irradiance of the Moon", *Astronom. J.* 129, 2887-2901 (2005).
40. T.C. Stone and H.H. Kieffer, "Assessment of Uncertainty in ROLO Lunar Irradiance for On-orbit Calibration", *Proc. SPIE* 5542, 300-310 (2004).
41. A. Wu, J. Mclntire, X. Xiong, F. J. De Luccia, H. Oudrari, D. Moyer, S. Xiong, and C. Pan, “Comparison of VIIRS pre-launch RVS performance using results from independent studies,” *Proc. SPIE,* 8153, 81530L (2011).
42. J. Sun, M. Wang, L. Tan, L. Jiang, “An Efficient Approach for VIIRS RDR to SDR Data Processing”, IEEE. Trans. Geosci. Remote Sens. Lett., 11, 2037-2041, 2014.
43. M. Wang, “A sensitivity study of SeaWiFS atmospheric correction algorithm: Effects of spectral band variations,” Remote Sens. Environ. 67, 348–359 (1999).
44. M. Wang and B. A. Franz, “Comparing the ocean color measurements between MOS and SeaWiFS: A vicarious intercalibration approach for MOS,” IEEE Trans. Geosci. Remote Sens. 38, 184–197 (2000).
45. M. Wang, A. Isaacman, B. A. Franz, and C. R. McClain, “Ocean color optical property data derived from the Japanese Ocean Color and Temperature Scanner and the French Polarization and Directionality of the Earth’s Reflectances: A comparison study,” Appl. Opt. 41, 974–990 (2002).
46. IOCCG, “Mission Requirements for Future Ocean-Colour Sensors,” C. R. McClain and G. Meister (Eds.), *Reports of International Ocean-Colour Coordinating Group*, No. 13 (IOCCG, Dartmouth, Canada, 2012).
47. D. Clark, H. Gordon, K. Voss, W. Broenkow, C. Trees, et al. (1997), “Validation of atmospheric correction over the oceans,” *Journal of Geophysical Research*, 102, 17209-17217 (1997).

48. D. Clark, M. Yarbrough, M. Feinholz, et al, “MOBY, a radiometric buoy for performance monitoring and vicarious calibration of satellite ocean color sensors: measurement and data analysis protocols,” in J. Mueller, G. Fargion, C. McClain, *Ocean Optics Protocols for Satellite Ocean Color Sensor Validation* **VI** (Revision 4 ed.), Greenbelt, MD: National Aeronautics and Space Administration Goddard Space Flight Center (2003), pp. 3–34, NASA/TM-2003-211621/Rev4-Vol.VI, retrieved 2008-11-21

Figure Captions

Table 1. VIIRS RSB and SDSM Specification

SDSD Detector	CW* (nm)	VIIRS Band	CW* (nm)	Band Gain
D1	412	M1	410	DG
D2	450	M2	443	DG
D3	488	M3	486	DG
D4	555	M4	551	DG
NA	NA	I1	640	SG
D5	672	M5	671	DG
D6	746	M6	745	SG
D7	865	M7	862	DG
D7	865	I2	862	SG
D8	935	NA	NA	NA
NA	NA	M8	1238	SG
NA	NA	M9	1378	SG
NA	NA	M10	1610	SG
NA	NA	I3	1610	SG
NA	NA	M11	2250	SG

*CW: Center Wavelength; DG: Dual Gain; SG: Singla Gain

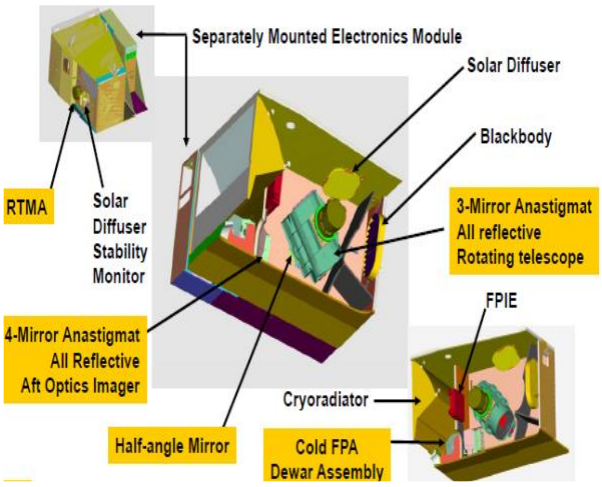

Fig. 1. VIIRS instrument and its on-board calibrators.

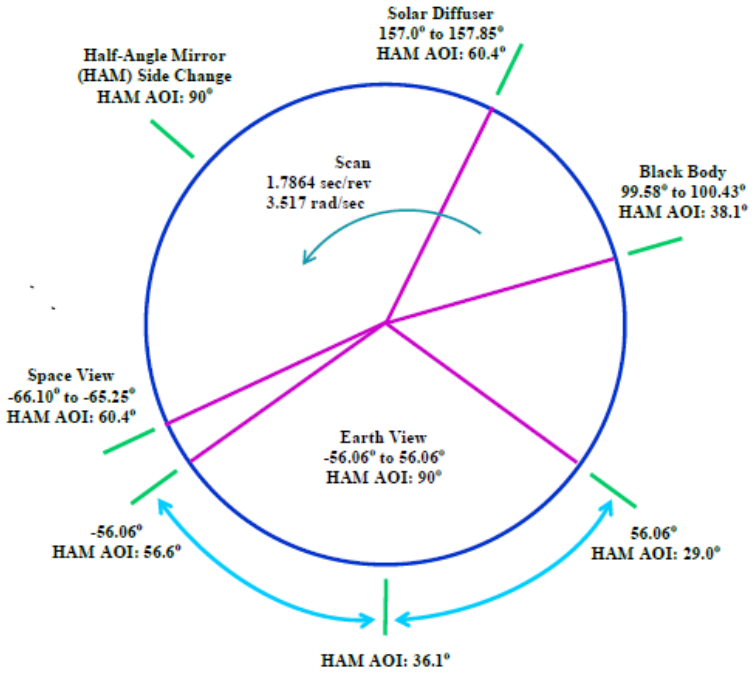

Fig. 2. Scan angles of VIIRS view sectors and their corresponding AOIs on the HAM.

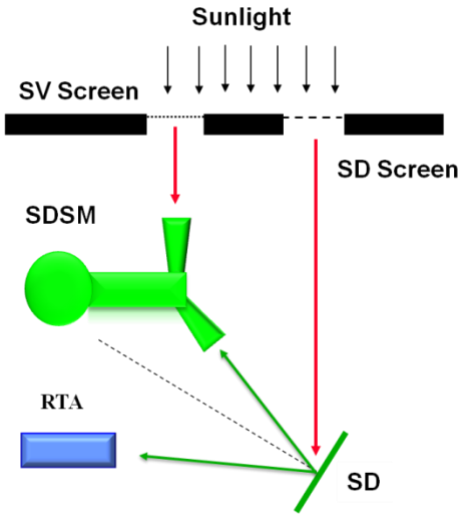

Fig. 3. Schematic diagram for SD/SDSM calibration.

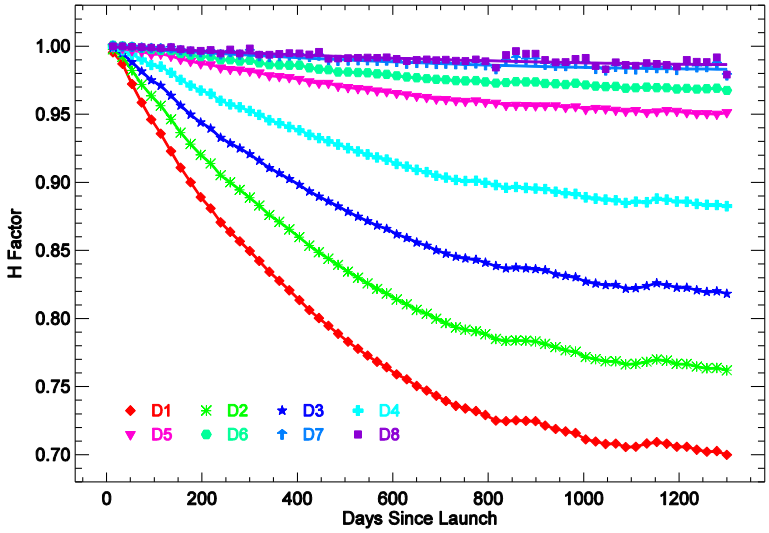

Fig. 4. SD degradation derived from the SDSM measurements.

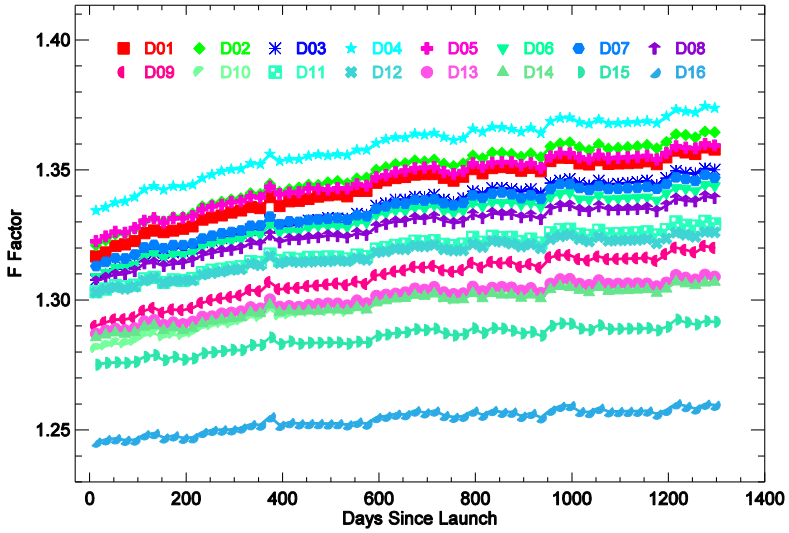

Fig. 5. VIIRS band M1 SD F-factors.

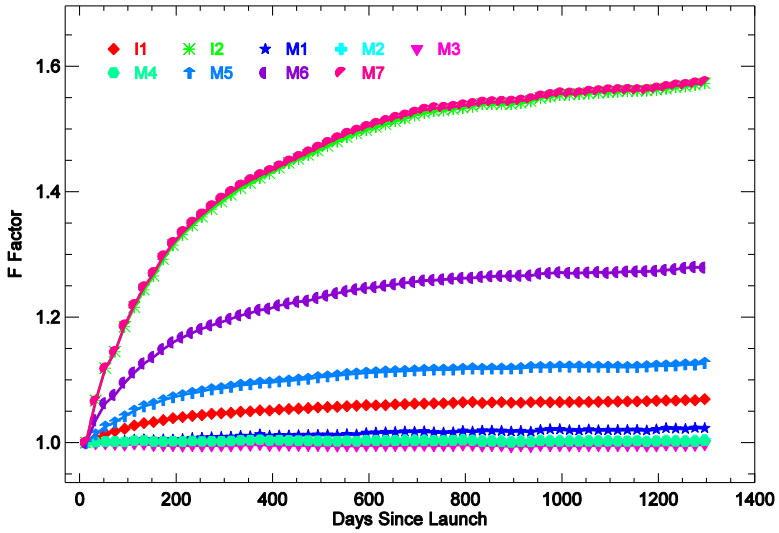

Fig. 6. VIIRS band averaged SD F-factors.

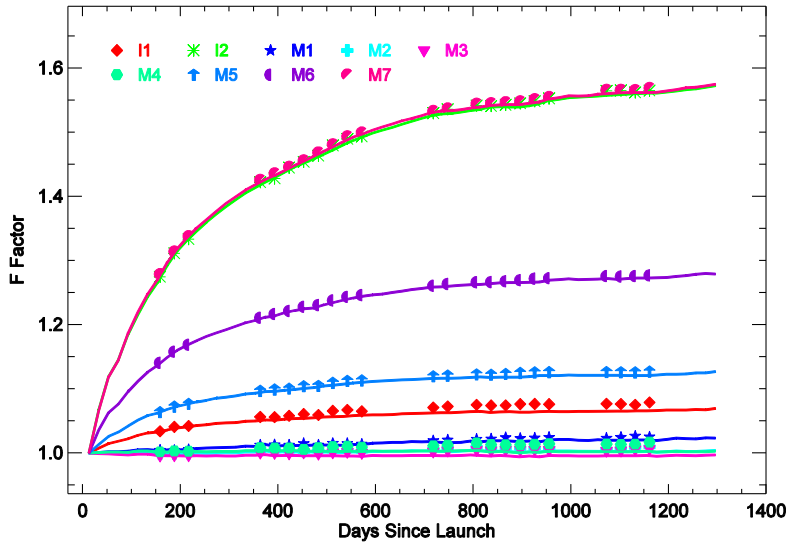

Figure 7. SNPP VIIRS RSB SD F-factors (lines) and lunar F-factors (symbols).

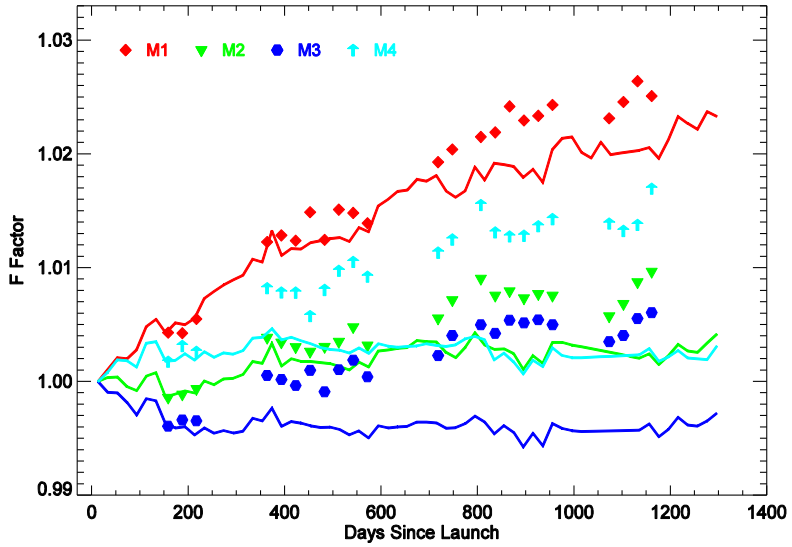

Figure 8. SNPP VIIRS RSB SD F-factors (lines) and lunar F-factors (symbols).

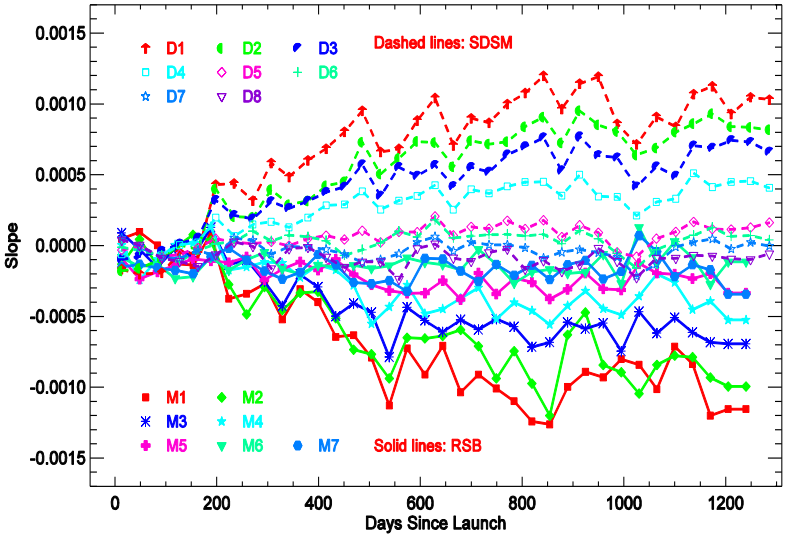

Fig. 9. Slopes of H-factors and F-factors in each individual event with respect to solar declination.

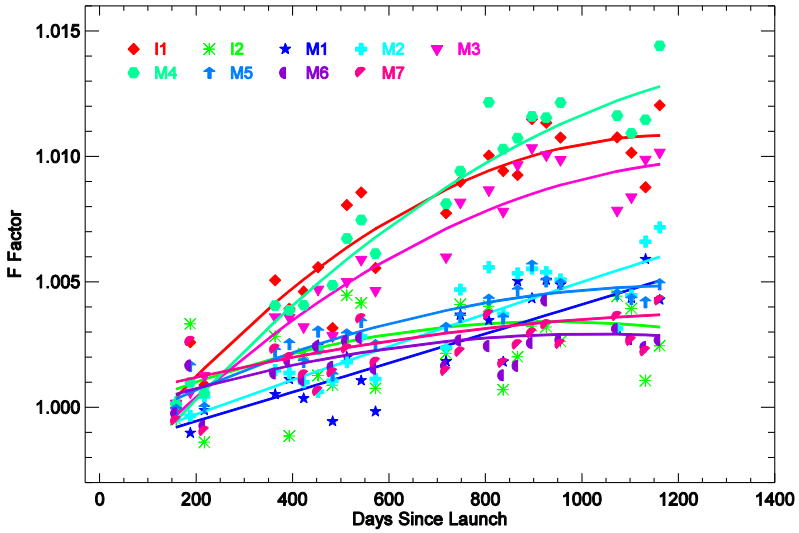

Fig. 10. Ratios of lunar F-factors over SD F-factors.

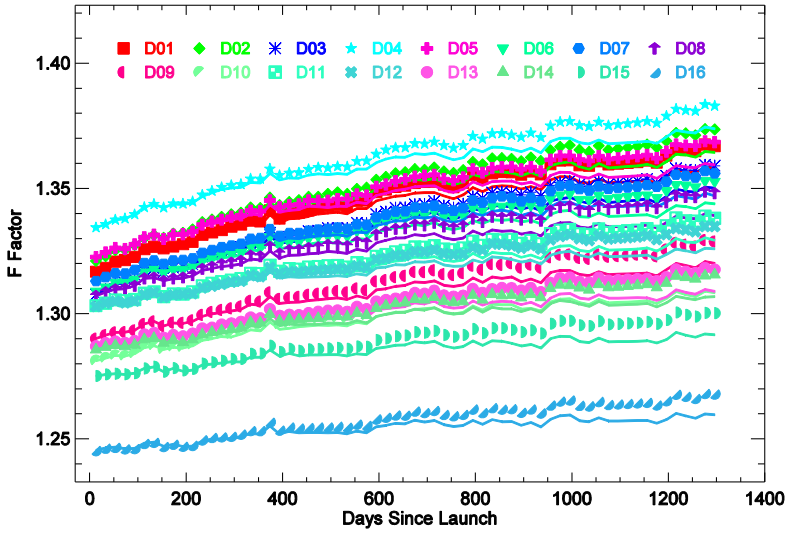

Fig. 11. Hybrid F-factors (symbols) and SD F-factors (lines) for the band M1.

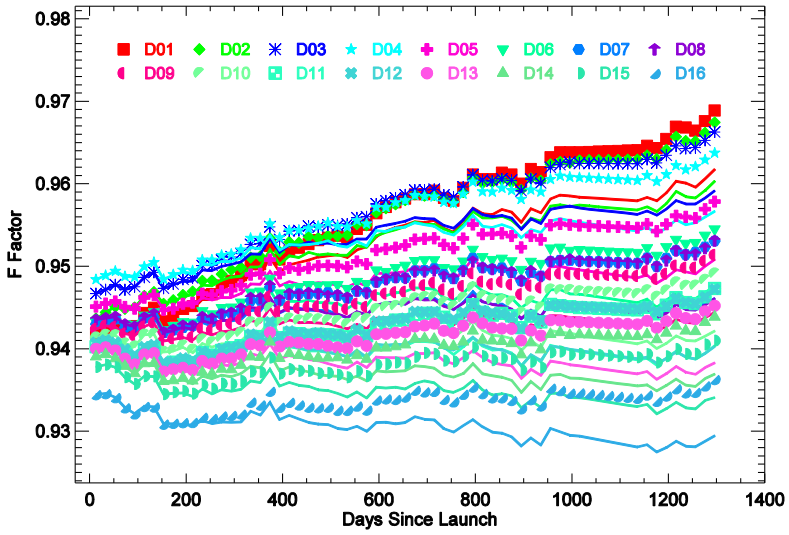

Fig. 12. Hybrid F-factors (symbols) and SD F-factors (lines) for the band M2.

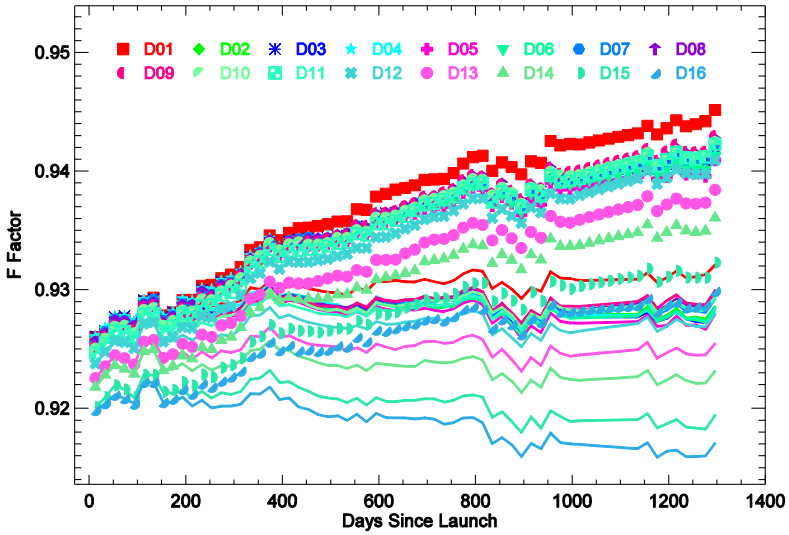

Fig. 13. Hybrid F-factors (symbols) and SD F-factors (lines) for the band M4.

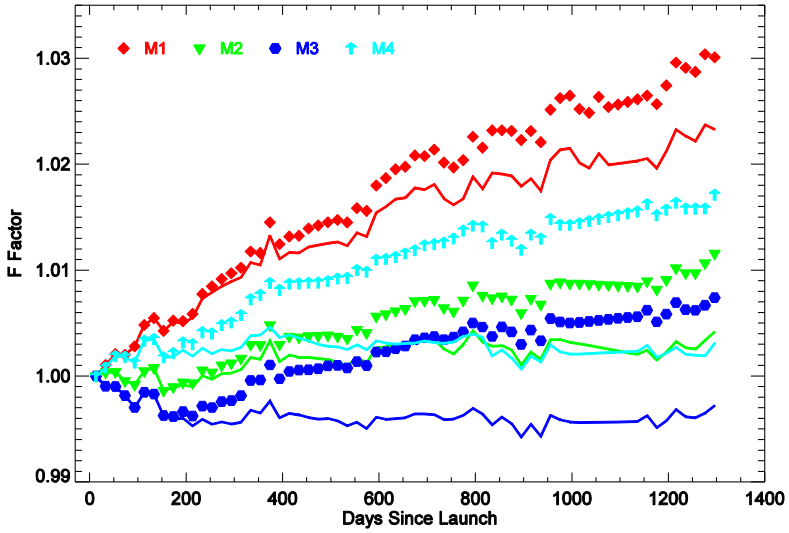

Fig. 14. Band averaged hybrid F-factors (symbols) and band averaged SD F-factors (lines).

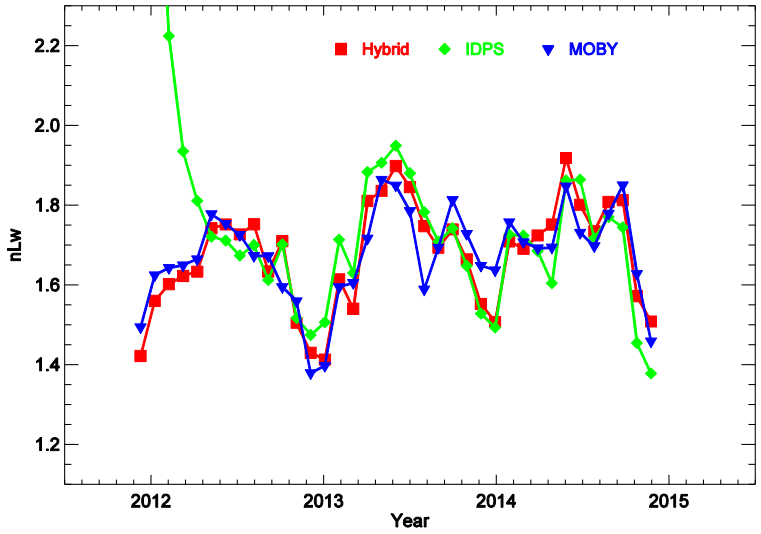

Fig. 15. Ocean $nL_w(\lambda)$ trending for the band M2 along with MOBY in-situ data.

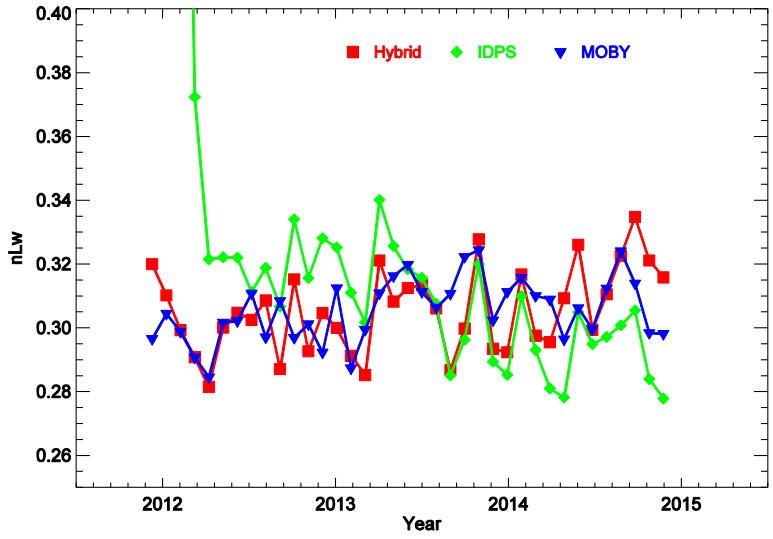

Fig. 16. Ocean $nL_w(\lambda)$ trending for the band M4 along with MOBY in-situ data.

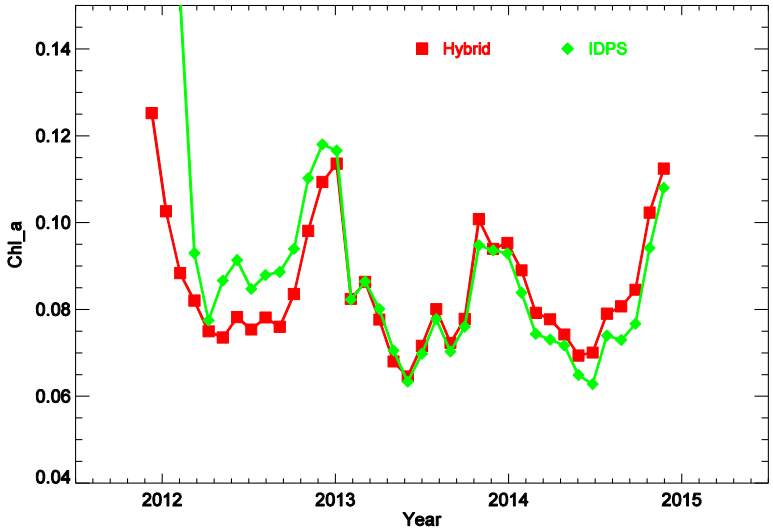

Fig. 17. Ocean Chl-a trending.